PHYSICAL REVIEW B **110**, 094102 (2024)

Continuous crossover between insulating ferroelectrics and polar metals: *Ab initio* calculation of structural phase transitions of LiBO$_3$ (B = Ta, W, Re, Os)

Ryota Masuki,[1,*] Takuya Nomoto,[2,†] Ryotaro Arita,[3,4,‡] and Terumasa Tadano[5,§]
[1]*Department of Applied Physics, The University of Tokyo, 7-3-1 Hongo, Bunkyo-ku, Tokyo 113-8656, Japan*
[2]*Department of Physics, Tokyo Metropolitan University, Hachioji, Tokyo 192-0397, Japan*
[3]*Department of Physics, The University of Tokyo, 7-3-1 Hongo, Bunkyo-ku, Tokyo 113-0033, Japan*
[4]*RIKEN Center for Emergent Matter Science, 2-1 Hirosawa, Wako, Saitama 351-0198, Japan*
[5]*CMSM, National Institute for Materials Science (NIMS), 1-2-1 Sengen, Tsukuba, Ibaraki 305-0047, Japan*

(Received 28 May 2024; revised 8 August 2024; accepted 13 August 2024; published 3 September 2024)

Inspired by the recent discovery of a new polar metal LiReO$_3$ by K. Murayama *et al*, we calculate the temperature (T)-dependent crystal structures of LiBO$_3$ with B = Ta, W, Re, Os, using the self-consistent phonon (SCPH) theory. We have reproduced the experimentally observed polar-nonpolar structural phase transitions and the transition temperatures (T_c) of LiTaO$_3$, LiReO$_3$, and LiOsO$_3$. From the calculation, we predict that LiWO$_3$ is a polar metal, which is yet to be tested experimentally. Upon doping electrons to the insulating LiTaO$_3$, the predicted T_c is quickly suppressed and approaches those of the polar metals. Thus, there is a continuous crossover between ferroelectric insulators and polar metals if we dope electrons to the ferroelectric insulators. Investigating the detailed material dependence of the interatomic force constants (IFCs), we explicitly show that the suppression of T_c in polar metals can be ascribed to the screening of the long-range Li-O interaction, which is caused by the presence of the itinerant electrons. The quantitative finite-temperature calculations do not show signs of unscreened long-range interactions by the weak electron-phonon coupling or enhancement of polar instabilities by carrier doping, as expected in some previous works.

DOI: 10.1103/PhysRevB.110.094102

I. INTRODUCTION

Polar metals, metals that show ferroelectriclike phase transition in terms of crystal symmetry, have attracted considerable interest since LiOsO$_3$ was experimentally identified as a polar metal for the first time [1]. With the coexistence of broken inversion symmetry and metallic conductivity, polar metals can host emergent phenomena [2] such as superconductivity [3,4], enhanced thermoelectricity [5,6], nontrivial topology [7,8], and multiferroicity [9].

However, only a few materials have been discovered [2,10,11], although half a century has passed since its first proposal [12]. This is because the long-range Coulomb interaction between local dipoles, which causes the ferroelectric instabilities in insulators [13,14], is screened out by the itinerant electrons. Thus, understanding the mechanism to overcome this incompatibility between polar instability and metalicity is essential to designing and discovering new polar metals with desired properties.

As the first discovered polar metal, LiOsO$_3$ has been extensively investigated experimentally and theoretically. LiOsO$_3$ shows second-order order-disorder structural phase transition between $R3c$ and $R\bar{3}c$ structures at 140 K [1,15–18]. In the high-temperature $R\bar{3}c$ phase, the ferroelectriclike A_{2u} phonon is unstable, which is dominated by the displacements of the Li ions. The origin of this instability has been discussed from different viewpoints, such as instability of Li and O ions [19,20], short-range geometric and bonding properties [21,22], the decoupling electron mechanism [23,24], incomplete screening of the dipole-dipole interaction [25], and hyperferroelectricity [26,27]. Some other materials have been investigated as well [24,28,29], but these works focus on individual materials and systematic investigations have been lacking because of the minimal number of known materials.

In addition, doping carriers to ferroelectric insulators has been investigated as an effective way to design a polar metal [30–33]. Some works predict that the polar atomic displacements are not suppressed and even enhanced by doping in many materials, which are attributed to the so-called metascreening effect [31,32]. However, they do not consider the finite-temperature effects. Furthermore, they focus on the relations of the ferroelectric insulators and doped ferroelectrics, but the relations between the intrinsic polar metals and these two remain unclear.

Recently, LiReO$_3$ have been experimentally revealed to be a polar metal [34]. LiReO$_3$ is isostructural to LiOsO$_3$ and shows a polar-nonpolar structural phase transition between the high-temperature $R\bar{3}c$ and the low-temperature $R3c$ phases at 170 K, which are shown in Fig. 1. In addition, LiTaO$_3$, another material in the LiBO$_3$ group with a 5d transition metal at the B site, has been reported to be a ferroelectric insulator. Therefore, we consider that LiBO$_3$ (B = 5d transition metals) is

---

[*] Contact author: masuki-ryota774@g.ecc.u-tokyo.ac.jp

[†] Contact author: tnomoto@tmu.ac.jp

[‡] Contact author: arita@riken.jp

[§] Contact author: tadano.terumasa@nims.go.jp

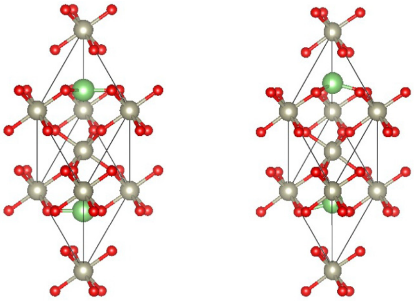

Nonpolar $R\bar{3}c$ Polar $R3c$

FIG. 1. The crystal structure of $\mathrm{LiReO_3}$ in the nonpolar $R\bar{3}c$ phase and in the polar $R3c$ phase. The figure of the crystal structures is generated by VESTA [57].

an ideal platform to perform systematic analysis on the polar metals and to investigate the relations between ferroelectrics, doped ferroelectrics, and polar metals.

In this work, we focus on $\mathrm{Li}B\mathrm{O_3}$ with B = Ta, W, Re, and Os. From the basic electronic-structure calculations, we have confirmed that $\mathrm{LiTaO_3}$ is an insulator while the other three are all metals in both the polar and nonpolar phases. The harmonic phonon calculations show that the A_{2u} mode at Γ point has the largest instability in the nonpolar $R\bar{3}c$ phase, which is consistent with the structural phase transitions of $\mathrm{LiTaO_3}$, $\mathrm{LiReO_3}$, $\mathrm{LiOsO_3}$.

Furthermore, we calculate the T dependence of the crystal structures of these materials based on the self-consistent phonon theory [35]. The calculated transition temperatures accurately reproduce the chemical trend. Based on the electronic, phononic, and the structural calculations, we predict that $\mathrm{LiWO_3}$ is another polar metal whose T_c is slightly lower than $\mathrm{LiReO_3}$ and $\mathrm{LiOsO_3}$. The synthesis of $\mathrm{LiWO_3}$ has been reported [36] but its detailed properties has not been measured yet. Upon doping electrons to the insulating $\mathrm{LiTaO_3}$, the high T_c is swiftly but continuously suppressed and approaches those of polar metals. Thus, there is a continuous crossover between the ferroelectric insulator and the polar metals, which are connected by the doped ferroelectrics. The result shows that the polar instability is suppressed with electron doping if we consider the finite temperatures, although the magnitude of the polar displacement remains intact (metascreening effect) [32]. Analyzing the interatomic force constants (IFCs) in detail, we explicitly show that the suppression of T_c in polar metals is caused by the screening of the long-range Li-O interactions. The calculation results suggest that the decoupling electron scenario that the long-range Coulomb interactions are only weakly coupled if the coupling between the electrons and polar mode is small [24] is not the case for these materials.

II. THEORY

We use the structural optimization method based on self-consistent phonon (SCPH) theory [35] to calculate the temperature dependence of the crystal structures. SCPH theory is a mean-field theory of the phonon anharmonicity, which has been demonstrated to accurately reproduce finite-temperature properties of strongly anharmonic materials [37–42].

SCPH theory is based on the variational principle of the free energy

$$\mathcal{F} = -k_BT\log \mathrm{Tr}e^{-\beta\hat{\mathcal{H}}_0} + \langle \hat{H} - \hat{\mathcal{H}}_0\rangle_{\hat{\mathcal{H}}_0} \geqslant F, \tag{1}$$

where F is the true free energy, and $\mathcal{F}$ is the variational free energy. $\hat{H}$ is the true Hamiltonian, and $\hat{\mathcal{H}}_0$ is the trial Hamiltonian, which we restrict to be a harmonic Hamiltonian $\hat{\mathcal{H}}_0 = \sum_{\boldsymbol{k}\lambda}\hbar\Omega_{\boldsymbol{k}\lambda}(\hat{a}^\dagger_{\boldsymbol{k}\lambda}\hat{a}_{\boldsymbol{k}\lambda} + \frac{1}{2})$ in SCPH theory. The SCPH frequencies $\Omega_{\boldsymbol{k}\lambda}$ are considered as the variational parameters, which are adjusted to minimize $\mathcal{F}$.[1] The minimization is performed by solving a self-consistent equation of $\Omega_{\boldsymbol{k}\lambda}$ [43], which we call the SCPH equation.

In structural optimization, we consider the minimized variational free energy ($\min_{\Omega_{\boldsymbol{k}\lambda}}\mathcal{F}$) as the approximate free energy and minimize it with respect to the crystal structures. We start from the Taylor expansion of the potential energy surface

$$\hat{U} = \sum_{n=0}^{\infty}\hat{U}_n, \tag{2}$$

$$\begin{aligned}\hat{U}_n &= \frac{1}{n!}\sum_{\{\boldsymbol{R}\alpha\mu\}}\Phi_{\mu_1\cdots\mu_n}(\boldsymbol{R}_1\alpha_1,\cdots,\boldsymbol{R}_n\alpha_n)\hat{u}_{\boldsymbol{R}_1\alpha_1\mu_1}\cdots\hat{u}_{\boldsymbol{R}_n\alpha_n\mu_n}\\ &= \frac{1}{n!}\frac{1}{N^{n/2-1}}\sum_{\{\boldsymbol{k}\lambda\}}\delta_{\boldsymbol{k}_1+\cdots+\boldsymbol{k}_n}\widetilde{\Phi}(\boldsymbol{k}_1\lambda_1,\cdots,\boldsymbol{k}_n\lambda_n)\hat{q}_{\boldsymbol{k}_1\lambda_1}\cdots\hat{q}_{\boldsymbol{k}_n\lambda_n},\end{aligned} \tag{3}$$

where $\hat{u}_{\boldsymbol{R}\alpha\mu}$ is the $\mu(= x, y, z)$ component of atomic displacement of atom α in the primitive cell at $\boldsymbol{R}$, and

$$\hat{q}_{\boldsymbol{k}\lambda} = \frac{1}{\sqrt{N}}\sum_{\boldsymbol{R}\alpha\mu}e^{-i\boldsymbol{k}\cdot\boldsymbol{R}}\epsilon^*_{\boldsymbol{k}\lambda,\alpha\mu}\sqrt{M_\alpha}\hat{u}_{\boldsymbol{R}\alpha\mu} \tag{4}$$

are those in the normal coordinate representation. $\epsilon_{\boldsymbol{k}\lambda,\alpha\mu}$ is the polarization vector of the phonon with mode λ and crystal momentum $\boldsymbol{k}$. M_α is the mass of the atom α. We call the Taylor expansion coefficients $\Phi_{\mu_1\cdots\mu_n}(\boldsymbol{R}_1\alpha_1,\cdots,\boldsymbol{R}_n\alpha_n)$ and $\widetilde{\Phi}(\boldsymbol{k}_1\lambda_1,\cdots,\boldsymbol{k}_n\lambda_n)$ as interatomic force constants (IFCs).

The IFCs are the functions of atomic positions in the unit cell, which we denote as $X_{\alpha\mu}$ for the $\mu(= x, y, z)$ component of the atomic position of atom α.[2] As the solution of the SCPH equation is determined by the set of IFCs $\widetilde{\Phi}$, we can write down the SCPH free energy as

$$F_{\mathrm{SCPH}}(X_{\alpha\mu}) = \mathcal{F}(\widetilde{\Phi}(X_{\alpha\mu}), \Omega_{\boldsymbol{k}\lambda}(\widetilde{\Phi}(X_{\alpha\mu}))). \tag{6}$$

The crystal structure ($X_{\alpha\mu}$) dependence of the IFCs $\widetilde{\Phi}$ can be calculated using the IFC renormalization [35,44,45]. Thus, we

---

[1] We treat the polarization vectors $\epsilon_{\boldsymbol{k}\lambda,\alpha\mu}$ as variational parameters as well. However, we explain the case in the fixed-mode approximation for simplicity. Please see Ref. [35] for detailed discussion.

[2] In Refs. [35,44], we express the atomic positions by the displacements from the reference positions in the normal coordinate representation, which we write as $q^{(0)}_\lambda$. If we denote the atomic coordinates in the reference structure as $X^{(\mathrm{ref})}_{\alpha\mu}$, these quantities are connected by the relation

$$q^{(0)}_\lambda = \sum_{\alpha\mu}\epsilon_{\boldsymbol{0}\lambda,\alpha\mu}\sqrt{M_\alpha}(X_{\alpha\mu} - X^{(\mathrm{ref})}_{\alpha\mu}). \tag{5}$$

TABLE I. The lattice constants that are used in the phonon calculations. The lattice constants are defined so that the lattice vectors of the conventional cell are $(a, 0, 0)$, $(-a/2, \sqrt{3}a/2, 0)$, $(0, 0, c)$. The conventional cells of LiBO$_3$ contain 30 atoms.

Materials	a [Å]	c [Å]
LiNbO$_3$ [34]	5.1818	13.6313
LiTaO$_3$	5.1885	13.6659
LiWO$_3$	5.1744	13.5222
LiReO$_3$ [34]	5.1267	13.3700
LiOsO$_3$	5.1116	13.0105

can calculate the gradient of the SCPH free energy $\frac{\partial F_{\mathrm{SCPH}}(X_{\alpha\mu})}{\partial X_{\alpha\mu}}$ and perform structural optimization with finite-temperature effects. Please see Refs. [35,44] for more details on the IFC renormalization and the structural optimization at finite temperatures.

III. SIMULATION DETAILS

A. Phonon calculations and structural optimizations at finite temperatures

We use the ALAMODE implementation of the SCPH calculation and SCPH-based structural optimization [35,43,44,46,47]. We use the $2 \times 2 \times 2$ supercell that contains 80 atoms in the phonon calculations. Note that supercells used in the calculations are based on the primitive cell, which is given by the parallelepiped shown in Fig. 1. The reference structure is determined using the structural optimization of VASP, whose lattice constants are summarized in Table I.

The harmonic IFCs are calculated using the small displacement method with atomic displacements of 0.01 Å. The anharmonic IFCs are obtained using the compressive sensing method [43,48], which enables efficient extraction of IFCs from a small number of displacement-force data. The displacement-force data is obtained with high-accuracy DFT calculations on a set of randomly displaced configurations. We use the *ab initio* molecular dynamics (AIMD) simulation to generate the randomly displaced configurations. We perform the AIMD calculation at 300 K for 16000 steps with the step of 1 fs for LiWO$_3$, LiReO$_3$, and LiOsO$_3$. The first 1000 steps are discarded as thermalization steps, and 300 snapshots are sampled uniformly from the rest 15000 steps. The configurations are generated by adding random atomic displacements of 0.04 Å to the 300 AIMD snapshots. The procedure is similar for LiNbO$_3$ and LiTaO$_3$. For these ferroelectric insulators, however, we perform AIMD calculations at 500 K and 750 K for 8000 steps, respectively. In each AIMD calculation, the first 1000 steps are discarded as thermalization steps, and 140 configurations are similarly extracted. Thus, we get 280 displacement-force data for LiNbO$_3$ and LiTaO$_3$, respectively. We choose the calculation settings so that the generated configurations effectively sample the low-energy region of the potential energy surface. Note that high accuracy is not necessary in the AIMD calculations because they are just for generating random structures.

We use $8 \times 8 \times 8$ q mesh in SCPH calculations. We fix the shape of the unit cell in SCPH-based structural optimizations because the cell volumes of the considering polar metals do not drastically change on structural phase transitions [1,34].

B. DFT calculations

We employ the Vienna *Ab initio* Simulation Package (VASP) [49] for DFT calculations. We use the PBEsol exchange-correlation functional [50] and the PAW pseudopotentials [51,52]. In the high-accuracy calculations, we set the convergence criteria of the SCF loop as 10^{-8} eV and the basis cutoff as 600 eV. We use the $4 \times 4 \times 4$ Monkhorst-Pack k mesh and accurate precision mode, which suppresses egg-box effects and errors. In the AIMD calculations, we set the convergence criteria of the SCF loop as 10^{-6} eV and the basis cutoff as 400 eV. We use the $2 \times 2 \times 2$ Monkhorst-Pack k mesh to reduce the computational cost. In both calculations, we use Gaussian smearing with a width of 0.05 eV. The spin-orbit coupling (SOC) is not included in the anharmonic phonon calculations because it does not affect the low-energy landscape of the potential energy surface [53].

In addition, we would like to add a short discussion on electronic correlations. The target materials LiBO$_3$ can be strongly correlated electron systems due to the 5d transition metals in the B site. In particular, electronic correlations of LiOsO$_3$ have been shown to be essential to precisely describe the electronic properties [54–56]. However, we do not explicitly consider the electronic correlations in this work. This is because the effect of electronic correlation will be the largest in LiOsO$_3$, which have half-filled t_{2g} bands, but it is not strong enough to cause metal-insulator transition. Thus, the conventional DFT calculations should be accurate enough to discuss distinctions between metals and insulators and basic electronic structures. Furthermore, previous works show that the electronic correlation little affects the structural properties [19], which is the main topic of this work.

IV. RESULTS AND DISCUSSION

A. Electronic structures of LiBO$_3$

We calculate the electronic structures of LiBO$_3$ with $B =$ Ta, W, Re, Os, which are shown in Fig. 2. All the materials show similar band structures with an almost isolated set of 12 bands (including spin degeneracy) near the Fermi level, which consist of hybridized B-site d orbitals and O p orbitals. LiTaO$_3$ is an insulator as the Fermi level lies in the middle of a band gap. As the number of 5d electrons increases, the Fermi level shifts upward, and the bands become half-filled in LiOsO$_3$. LiWO$_3$, LiReO$_3$, and LiOsO$_3$ are all metals. In the Supplemental Material [53], we summarize all the calculation results both on the high-T $R\bar{3}c$ and low-T $R3c$ phase, with and without SOC. According to Figs. S1–S4, LiTaO$_3$ is an insulator, while LiWO$_3$, LiReO$_3$, and LiOsO$_3$ are metals in the low-T $R3c$ phase as well. Thus, the metal-insulator transitions do not occur with the structural phase transitions in the target materials. This is consistent with the experimental observation that LiReO$_3$ is a polar metal [34], and supports our prediction that LiWO$_3$ is another polar metal, which we discuss later.

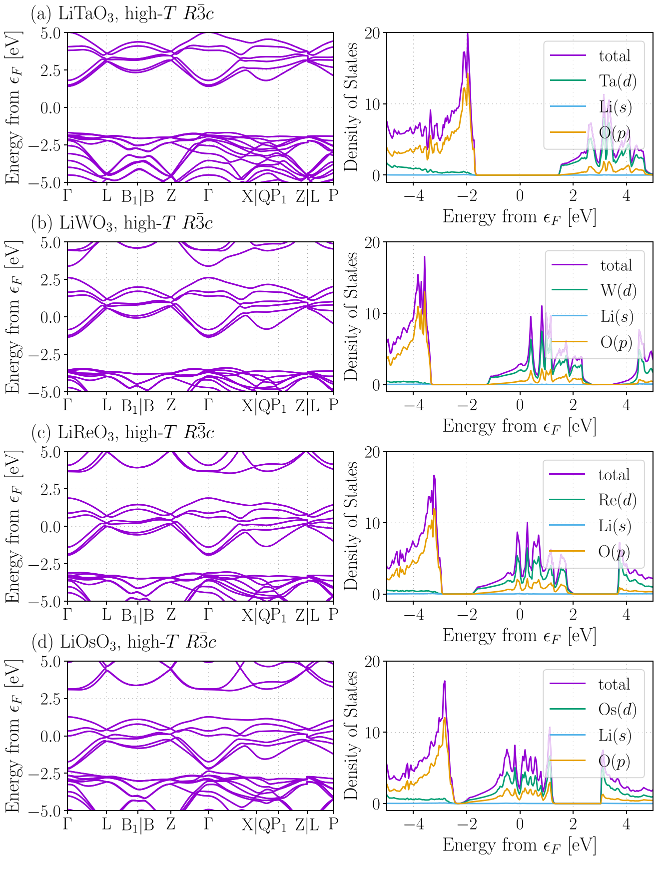

FIG. 2. The electronic band structures and density of states (DOS) of (a) LiTaO$_3$, (b) LiWO$_3$, (c) LiReO$_3$, (d) LiOsO$_3$. The calculations are performed on the high-temperature $R\bar{3}c$ phase, taking into account SOC.

B. Harmonic phonons of LiBO$_3$

We calculate the harmonic phonon dispersions and atom-projected phonon density of states of LiBO$_3$. Note that we neglect SOC from this section because SOC hardly affects the low-energy region of the potential energy surface, which we show in Sec. II in the Supplemental Material [53]. Figure 3 shows the calculation results of LiReO$_3$. LiReO$_3$ has a pair of unstable modes in the high-T $R\bar{3}c$ phase, which is dominated by Li ions. The most unstable mode is the ferroelectriclike A_{2u} mode at Γ point that causes the transition to the low-T $R3c$ phase, which is common to all B = Ta, W, and Os cases [53]. We also show the T dependence of the SCPH dispersion of the high-temperature phases of LiBO$_3$ in Sec. III of the Supplemental Material [53]. The ferroelectriclike mode at Γ point softens the most drastically as the temperature gets lower, which is also consistent with the polar-nonpolar structural phase transitions. The nondispersive nature of the soft modes in the harmonic dispersions suggests that the transition is caused by the on-site instability of the loosely bonded small Li ions, as suggested for LiOsO$_3$ [18,20]. The imaginary phonon is lifted in the low-temperature phase, and the instability disappears.

In Sec. IV A, we saw that the electronic bands of LiBO$_3$ near the Fermi level are dominated by the B-site d orbitals and O p orbitals, while the contribution of Li ions, which dominates the instability of the high-symmetry phase, is negligible. Thus, LiReO$_3$ seems consistent with the decoupling electron mechanism [24], that the electronic state near the Fermi level and the polar atomic displacements are decoupled, as discussed on LiOsO$_3$ [20,23].

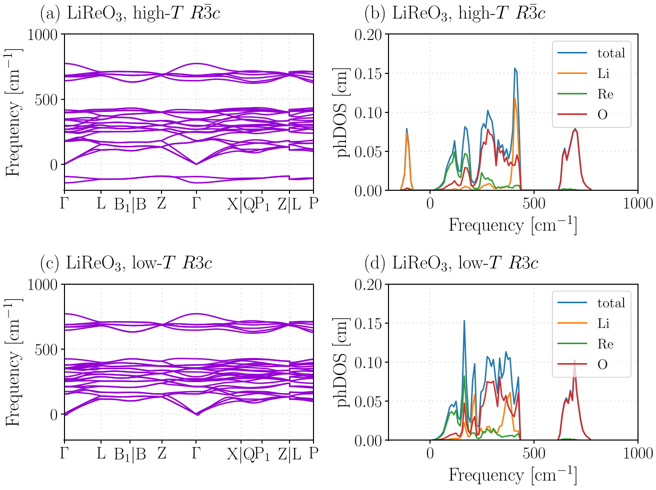

FIG. 3. Calculation results of the harmonic phonon dispersion and atom-projected phonon density of states of LiReO$_3$ in the high-T $R\bar{3}c$ phase and in the low-T $R3c$ phase.

C. Structural phase transitions of LiBO$_3$

Based on the above discussions, we apply the SCPH-based structural optimization at finite temperatures to LiBO$_3$ with B = Ta, W, Re, Os. The temperature dependence of the atomic displacements are shown in Fig. 4. The atomic displacements are defined with respect to the reference structure, which is obtained by the structural optimization at zero temperature based on DFT. The displacements of Li and B-site ions are zero at high temperatures, while they are finite at low temperatures.

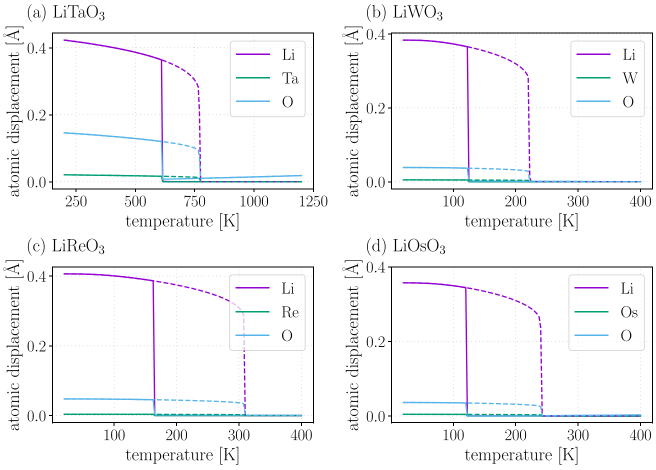

FIG. 4. Calculation results of the temperature dependence of the atomic displacements of LiBO$_3$ with B = (a) Ta, (b) W, (c) Re, (d) Os. The solid lines show the cooling calculations, in which we start from the high-temperature and add a slight atomic displacement along the unstable A_{2u} mode until the transition to the low-temperature phase is induced. The dashed lines show the heating calculations, in which we start from the low-temperature $R3c$ phase.

TABLE II. The calculated and experimental transition temperatures (T_c) of LiBO$_3$ with B = Nb, Ta, W, Re, Os.

Materials	calculation [K]	experiment [K]
$LiNbO_3$	1350 [34]	1480 [58]
$LiTaO_3$	723	910 [58]
$LiWO_3$	193	–
$LiReO_3$	267 [34]	170 [34]
$LiOsO_3$	207	140 [1]

The atomic displacements of O atoms can be finite in high-T phases because their internal positions are not completely fixed by symmetry. Hence, the polar-nonpolar structural phase transitions of these materials are reproduced by theoretical calculations. The transition temperatures, which are estimated from the crossing points of the SCPH free energies, are summarized in Table II. We can see that the calculated T_c of each material is compatible with the experimental values. In addition, the calculation results reproduce the chemical trend, i.e., T_c of the ferroelectric insulators (B = Nb, Ta) are much higher than those of polar metals (B = Re, Os). The chemical trends within each class (the ferroelectrics and the polar metals) are also accurately reproduced. The SCPH theory cannot treat the deviation of the atomic distribution function from the Gaussian distribution of the effective harmonic Hamiltonian. Thus, it is less suited for the order-disorder structural phase transition than for the displacive structural phase transitions. However, because the SCPH theory calculates the effective harmonic Hamiltonian based on the variational principle, we can expect that it approximates the spread of the atomic distributions around the average positions. In fact, the agreement of T_c with the experimental results suggests that the effective mean-field theory accurately captures the overall behavior of the materials. Such limitations of the SCPH theory can be one reason for the errors of calculated T_c.

As shown in Fig. S8 in the Supplemental Material [53], the ferroelectriclike A_{2u} mode that drives the polar-nonpolar structural phase transition has the largest instability in the high-temperature $R\bar{3}c$ phase of $LiWO_3$. In addition, $LiWO_3$ is metallic in both $R\bar{3}c$ and $R3c$ phases, which we can see from Fig. S2. Thus, we predict that $LiWO_3$ is another isostructural polar metal whose transition temperature T_c is slightly lower than $LiReO_3$ and $LiOsO_3$.

As depicted in Fig. 5, the calculated T_c of the polar metals LiBO$_3$ (B = W, Re, Os) do not change drastically with the number of d electrons per B site, while $LiTaO_3$ significantly deviates from this trend. Here, we focus on the region between the ferroelectric insulator and the polar metals. We dope electrons to the insulating $LiTaO_3$ by changing the number of electrons in DFT calculations and investigate the change of T_c. From Fig. 5, the T_c of $LiTaO_3$ is quickly suppressed and approaches those of polar metals upon electron doping. Note that such calculations to change the number of electrons are not necessarily accurate because of the possible artifact from the uniform positive background. In fact, we fix the shape of the unit cell when we change the number of electrons because the lattice constants optimized by DFT calculations largely deviate from the chemical trend. However, we consider the quick suppression of T_c in doped $LiTaO_3$ is qualitatively correct because T_c changes much more slowly and follows the trend when we reduce the number of electrons in $LiWO_3$, as shown in Fig. 5.

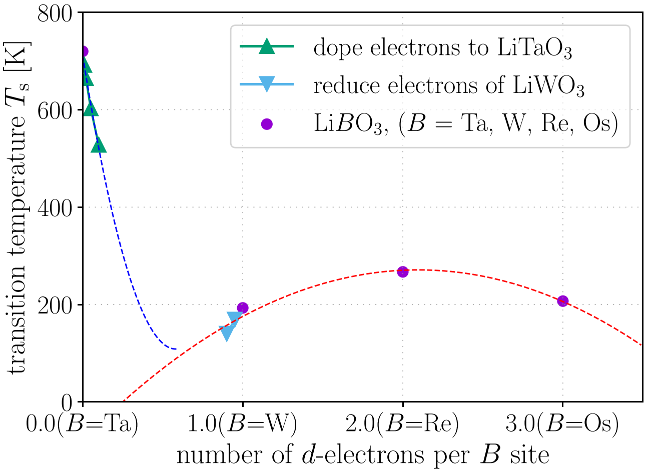

FIG. 5. The calculated transition temperatures of LiBO$_3$ with different numbers of electrons per B site. The dotted lines are guide to the eye.

Because the change of T_c is continuous, we consider that there is a continuous crossover between the ferroelectric insulators and the polar metals, which are connected by doped ferroelectrics. Upon doping electrons to ferroelectric insulators, the polar instabilities are suppressed at finite temperatures, even when the polar displacements at zero temperature remain unchanged.

D. Chemical trend of T_c in the polar metals LiBO$_3$

In this section, We discuss the origin of the trend of T_c of polar metals in Fig. 5. Up to the quartic order, the double well potential along the soft mode can be written as

$$U(q_\lambda) = \frac{1}{2}\widetilde{\Phi}(\mathbf{0}\lambda,\mathbf{0}\lambda)q_\lambda^2 + \frac{1}{4!}\widetilde{\Phi}(\mathbf{0}\lambda,\mathbf{0}\lambda,\mathbf{0}\lambda,\mathbf{0}\lambda)q_\lambda^4 \quad (7)$$

$$= \frac{1}{2}\widetilde{\Phi}_2 q_\lambda^2 + \frac{1}{4!}\widetilde{\Phi}_4 q_\lambda^4, \quad (8)$$

where we defined $\widetilde{\Phi}_2 = \widetilde{\Phi}(\mathbf{0}\lambda,\mathbf{0}\lambda)$ and $\widetilde{\Phi}_4 = \widetilde{\Phi}(\mathbf{0}\lambda,\mathbf{0}\lambda,\mathbf{0}\lambda,\mathbf{0}\lambda)$ for notational simplicity. q_λ is the atomic displacement along the ferroelectriclike soft mode in normal coordinate representation. The depth of this double well potential is $\frac{3\widetilde{\Phi}_2^2}{2\widetilde{\Phi}_4}$, which is roughly proportional to T_c as shown in Table III. In Table III, $T_{c,\mathrm{est}}$ are the transition temperatures estimated from the assumption that $T_c \propto \frac{3\widetilde{\Phi}_2^2}{2\widetilde{\Phi}_4}$ and T_c of $LiReO_3$ is 267 K. Since $T_{c,\mathrm{est}}$ reproduces the trend of the calculated transition temperatures $T_{c,\mathrm{calc}}$, we can conclude that the assumption $T_c \propto \frac{3\widetilde{\Phi}_2^2}{2\widetilde{\Phi}_4}$ holds approximately. Thus, the chemical trend of T_c of LiBO$_3$ can be explained by the change of $\widetilde{\Phi}_2$ and $\widetilde{\Phi}_4$ among these materials.

According to Table III, $\widetilde{\Phi}_4$ monotonically increases from B = Ta to B = Os. This is presumably because the quartic interaction arises from the short-range repulsive forces between ions, which generally get larger as the lattice constants get smaller. $|\widetilde{\Phi}_2|$ takes the largest value in $LiTaO_3$, which leads to the highest T_c among the target materials. In the polar metals, $|\widetilde{\Phi}_2|$ also monotonically increases from B = W to B = Os.

TABLE III. The interatomic force constants along the ferroelectriclike soft mode and the estimated transition temperatures. $\widetilde{\Phi}_2$ and $\widetilde{\Phi}_4$ are the IFCs along the soft mode ($\mathbf{0}\lambda$), which are defined as $\widetilde{\Phi}_2 = \widetilde{\Phi}(\mathbf{0}\lambda, \mathbf{0}\lambda)$ and $\widetilde{\Phi}_4 = \widetilde{\Phi}(\mathbf{0}\lambda, \mathbf{0}\lambda, \mathbf{0}\lambda, \mathbf{0}\lambda)$. $T_{c,\mathrm{est}}$ are the transition temperatures estimated from the assumption that $T_c \propto \frac{3\widetilde{\Phi}_2^2}{2\widetilde{\Phi}_4}$ and T_c of LiReO$_3$ is 267 K. $T_{c,\mathrm{calc}}$ is the T_c calculated by the SCPH-based structural optimization, which are also summarized in Table II.

	$\widetilde{\Phi}_2$ [Ry/(a_B^2 u)]	$\widetilde{\Phi}_4$ [Ry/(a_B^2 u)^2]	$T_{c,\mathrm{est}}$ [K]	$T_{c,\mathrm{calc}}$ [K]
LiTaO$_3$	-1.963×10^{-3}	0.706×10^{-3}	586	723
LiWO$_3$	-1.091×10^{-3}	0.741×10^{-3}	173	193
LiReO$_3$	-1.541×10^{-3}	0.955×10^{-3}	267	267
LiOsO$_3$	-1.591×10^{-3}	1.326×10^{-3}	205	207

If the instability originates from the competition of the short-range repulsion and the long-range dipole-dipole interaction, which is usually the case in ferroelectric insulators, the chemical trend of $\widetilde{\Phi}_2$ would be opposite because the short-range repulsion quickly gets prominent when the lattice constant shrinks. Thus, this B-site dependence of $|\widetilde{\Phi}_2|$ supports that the instability of the polar metals has a short-range origin, which has been suggested for LiOsO$_3$ in previous research [21].

E. Difference between ferroelectric insulators and polar metals

Lastly, we discuss the origin of the difference in the transition temperatures between the ferroelectric insulator LiTaO$_3$ and the polar metals LiBO$_3$ (B = W, Re, Os). In Fig. 6, we plot the z-z components of the interatomic force constants (IFCs) of the nth nearest-neighbor (NN) shells from a Li ion. z direction is defined along the c axis of the conventional cell of the rhombohedral structure. x and y axis are defined so that the xyz defines a rectangular coordinate system. Note that similar discussions can be done on other components of the IFCs, which is shown in Sec. V in the Supplemental Material [53]. The IFCs of different element pairs are plotted separately. The nth nearest-neighbor shell of the element pair Li-A is defined as the nth nearest group of A atoms when we fix a Li atom and classify the A atoms around it in terms of the distance from the fixed Li atom. The atomic distances of these nth nearest-neighbor shells of LiReO$_3$ are summarized in Table IV. The cases of B = Ta, W, Os are shown in Tables S2– S4 in the Supplemental Material [53], which are almost the same as the LiReO$_3$ case. Since the soft modes of LiBO$_3$ are dominated by Li and O displacements, let us consider the results of the element pairs Li-Li and Li-O [Fig. 6(a), 6(c)]. In fact, the contributions of the Li-B IFCs to the potential energy surface along the soft modes are small as we later discuss in this section. The short-range IFCs with atomic distances smaller than 3.0 Å [zeroth NN shell of Li-Li (Li on site) and first and second NN shell of Li-O] are finite in both the ferroelectric insulator and the polar metals. These IFCs seem to change almost linearly when the B-site ion is changed. On the other hand, the long-range IFCs, which we define as IFCs with atomic distances larger than 3.0 Å in this paper (e.g., third NN shell of Li-Li, third, fifth, and sixth NN shells of Li-O), are finite in LiTaO$_3$ but are close to zero in the polar metals.

This distinction between the short-range and long-range IFCs can be seen more clearly in Fig. 7, in which we plot the B dependence of the IFCs. As we see from Fig. 7(a), the short-range IFCs show systematic dependence on B site ions, and there is no apparent difference between the ferroelectric

(a) Li-Li IFC (z-z component)

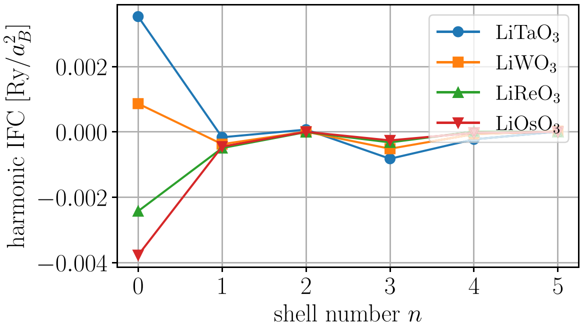

(b) Li-B IFC (z-z component)

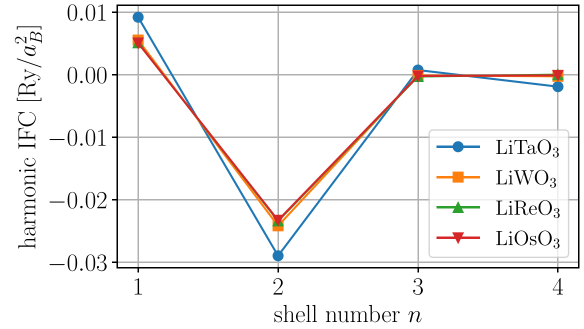

(c) Li-O IFC (z-z component)

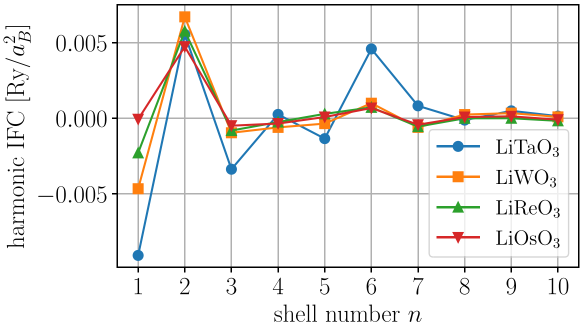

FIG. 6. The zz components of the interatomic force constants of the nth nearest-neighbor shells from a Li ion of LiBO$_3$ (B = Ta, W, Re, Os). The nth nearest-neighbor shells of the element pair Li-A is defined as the nth nearest group of A atoms when we fix a Li atom as the center and classify the A atoms around it in terms of the distance from the fixed Li atom. The plotted IFCs of the nth nearest-neighbor shell of the element pair Li-A is Φ_{zz} (center Li atom, $\boldsymbol{R}\alpha$), where nth $\boldsymbol{R}\alpha$ is included in the nearest-neighbor shell. Note that we consider the onsite IFC as the IFC of the zeroth nearest neighbor.

TABLE IV. nth nearest-neighbor shells from a Li ion of $LiReO_3$. The shell number n with the number of atoms in the nth NN shell, and the corresponding atomic distances. The results are calculated on the crystal structure in the high-temperature $R\bar{3}c$ phase without SOC. Note that the number of atoms in the shells are calculated within the $2 \times 2 \times 2$ supercell considering the periodic boundary condition.

	Li-Li	
shell number n	no. of atoms	distance (Å)
0	1	0.0000
1	6	3.7049
2	3	5.1267
3	3	5.3500
4	2	6.3253
5	1	7.4098

	Li-B	
shell number n	no. of atoms	distance (Å)
1	6	3.1626
2	2	3.3425
3	2	6.0237
4	6	6.1200

	Li-O	
shell number n	no. of atoms	distance (Å)
1	3	1.9852
2	6	2.7368
3	3	3.1414
4	6	4.2033
5	6	4.4773
6	6	4.7314
7	6	4.8574
8	6	5.2769
9	3	5.7065
10	3	6.2041

insulator and the polar metals. Figure 7(b) shows representative examples of long-range IFCs that have relatively large contributions. These long-range IFCs have a significant finite value in $LiTaO_3$, but they are small and almost constant in polar metals, which can ascribed to the screening of the Coulombic interaction by the itinerant electrons. Although we discuss the importance of O-O interactions in the Supplemental Material [53], we do not consider them here because it is difficult to choose important components such as z-z components. As the O sites have lower symmetry, their displacements in the soft mode are not along the z direction, and atoms that belong to the same nearest-neighbor shell can be displaced in different directions.

Furthermore, we apply cutoffs to the harmonic IFCs and investigate the change of instabilities along the ferroelectriclike soft modes. Figure 8 shows the cutoff dependence of the curvature of the potential energy surface. Here, we set the harmonic IFCs with atomic distance larger than the cutoff as zero and calculate

$$\frac{d^2U}{dq_\lambda^2} = \sum_{\mathrm{dist}(\mathbf{0}\alpha,\boldsymbol{R}_1\alpha_1)<\mathrm{cutoff}} \sum_{\mu\mu_1} \frac{\epsilon_{\mathbf{0}\lambda,\alpha\mu}}{\sqrt{M_\alpha}} \frac{\epsilon_{\mathbf{0}\lambda,\alpha_1\mu_1}}{\sqrt{M_{\alpha_1}}} \Phi_{\mu\mu_1}(\mathbf{0}\alpha, \boldsymbol{R}_1\alpha_1). \tag{9}$$

(a) short-range IFCs, z-z components

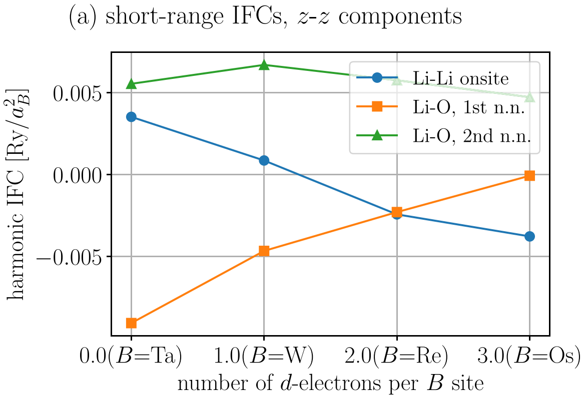

(b) long-range IFCs, z-z components

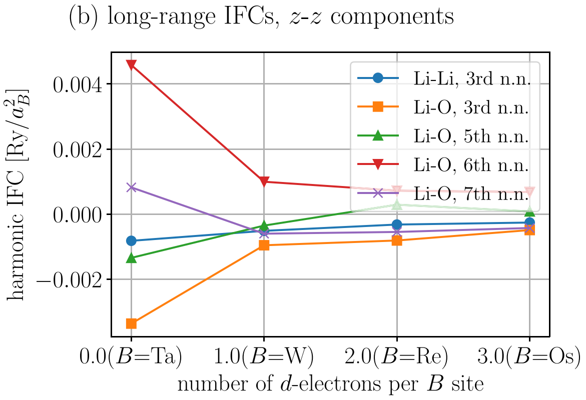

FIG. 7. B-site dependence of the z-z components of the interatomic force constants (IFCs) of nth nearest-neighbor (NN) shells of different element pairs. (a) The short-range IFCs with atomic distance smaller than 3 Å. (b) The long-range IFCs with atomic distance larger than 3 Å.

q_λ is the atomic displacement in normal coordinate representation along the soft mode, and the polarization vector of the soft mode $\epsilon_{\boldsymbol{k}\lambda,\alpha\mu}$ is fixed when the dynamical matrix is

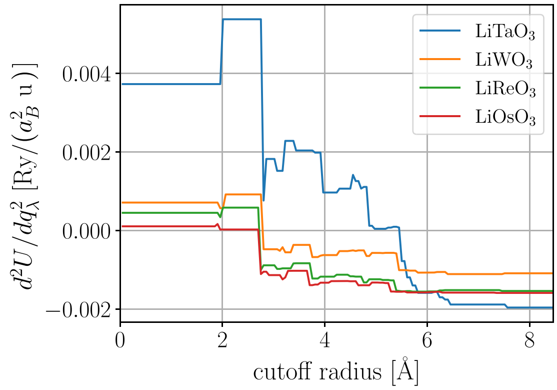

FIG. 8. Cutoff dependence of the curvature of the potential energy surface $\frac{d^2U}{dq_\lambda^2}$. We set the harmonic IFCs with the atomic distance larger than the cutoff as zero and calculate the curvature $\frac{d^2U}{dq_\lambda^2} = \sum'_{\alpha,\boldsymbol{R}_1\alpha_1,\mu\mu_1} \frac{\epsilon_{\mathbf{0}\lambda,\alpha\mu}}{\sqrt{M_\alpha}} \frac{\epsilon_{\mathbf{0}\lambda,\alpha_1\mu_1}}{\sqrt{M_{\alpha_1}}} \Phi_{\mu\mu_1}(\mathbf{0}\alpha, \boldsymbol{R}_1\alpha_1)$, where $\sum'$ is the sum restricted to the IFCs with atomic distance smaller than the cutoff radius. q_λ is the atomic displacement along the ferroelectriclike soft mode in normal-coordinate representation. The calculation is performed on the nonpolar $R\bar{3}c$ phase without SOC.

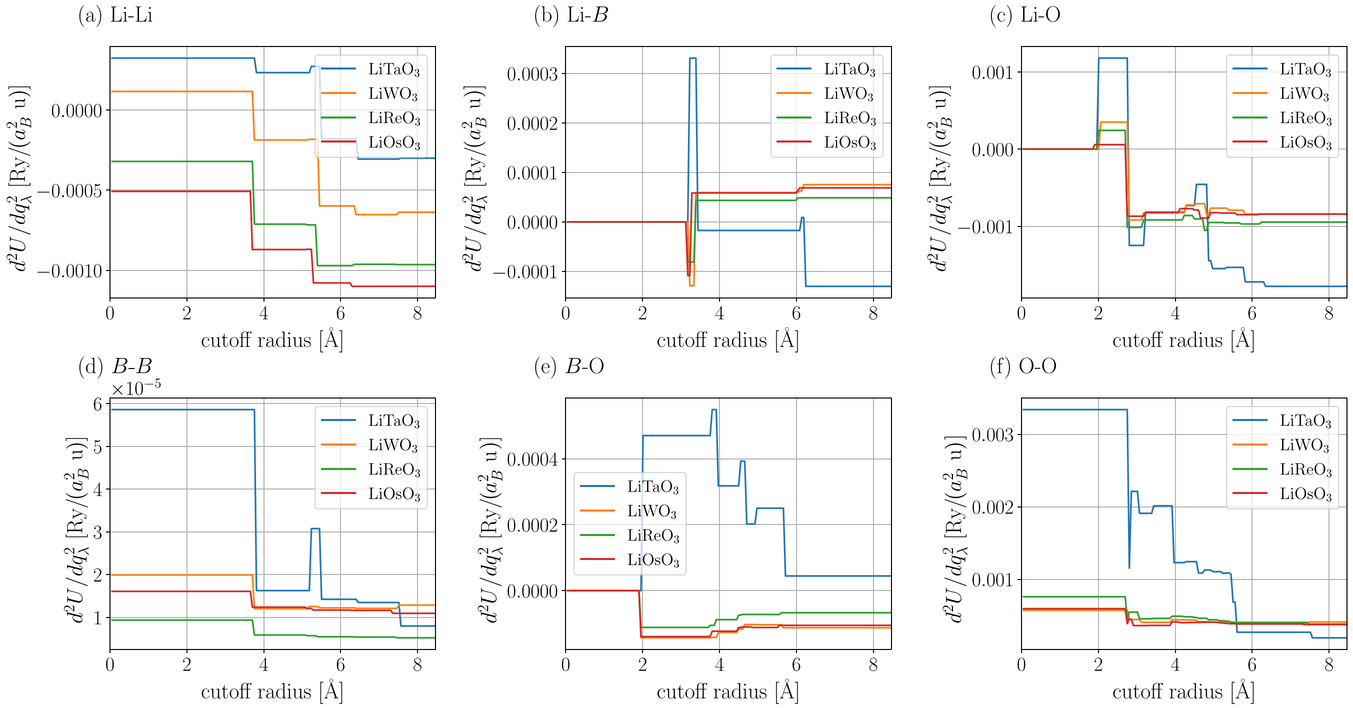

FIG. 9. Contributions from IFCs of different element pairs to the curvature of the potential energy surface $\frac{d^2U}{dq_\lambda^2}$. To calculate the cutoff radius dependence, we set the harmonic IFCs with the atomic distance larger than the cutoff as zero and calculate the curvature $\frac{d^2U}{dq_\lambda^2} = \sum'_{\alpha,\boldsymbol{R}_1\alpha_1,\mu\mu_1} \frac{\epsilon_{\mathbf{0}\lambda,\alpha\mu}}{\sqrt{M_\alpha}} \frac{\epsilon_{\mathbf{0}\lambda,\alpha_1\mu_1}}{\sqrt{M_{\alpha_1}}} \Phi_{\mu\mu_1}(\mathbf{0}\alpha, \boldsymbol{R}_1\alpha_1)$, where $\sum'$ is the sum restricted to the IFCs with atomic distance smaller than the cutoff radius. q_λ is the atomic displacement along the ferroelectriclike soft mode in normal-coordinate representation. The calculation is performed on the nonpolar $R\bar{3}c$ phase without SOC.

altered by applying the cutoff. In Fig. 8, the polar metals with B = W, Re, Os show similar behaviors. The instability ($\frac{d^2U}{dq_\lambda^2} < 0$) appears when the cutoff radius is around 3.0 Å and the curvature is almost constant when the cutoff is large. Thus, the polar instabilities of the polar metals are dominated by the short-range IFCs, and the contributions from the long-range IFCs are relatively small, consistent with the discussion in the last paragraph. On the other hand, the long-range IFCs have considerable contributions in LiTaO$_3$, where the largest instability appears only when the long-range IFCs are considered.

In Fig. 9, we separate the result of Fig. 8 to contributions from different element pairs. The contributions of the element pairs that contain B-site ions are small because the displacements of B-site ions are negligibly small in the soft modes of these materials as shown in Table S1 in the Supplemental Material [53]. The contribution of Li-Li IFCs [Fig. 9(a)] shows similar behaviors in all materials, and the instability gets monotonically more significant from B = Ta to B = Os. This is consistent with the B-site dependence of the on-site Li IFC that the Li site gets more unstable from B = Ta to B = Os, which is shown in Fig. 6(a) and Fig. 7(a). As shown in Fig. 9(c), the Li-O interactions are crucial to the largest instability and the highest T_c of LiTaO$_3$ among the target materials, to which the long-range IFCs have a significant contribution.

The short-range part of Fig. 8 shows clear difference between LiTaO$_3$ and the polar metals although the B-site dependence of the short-range IFCs is rather systematic as shown in Fig. 7(a). These seemingly contradicting results can be ascribed to the difference in the polarization vector. In Sec. VI in the Supplemental Material [53], we discuss that larger O contribution to the soft mode is essential to the large instability of LiTaO$_3$, for which the long-range Li-O and O-O interactions play an important role.

F. Discussion on the origin of structural phase transitions in polar metals

Here, we briefly discuss our understanding on the structural phase transitions of the polar metals in comparison with the previous works on LiOsO$_3$. We have clarified that the drastic suppression of T_c from the ferroelectric insulator LiTaO$_3$ to the polar metals are caused by the screening of the long-range IFCs, which is ascribed to the itinerant electrons. The polar instability of the polar metals originate from the short-range IFCs, which show linearlike dependence on B-site atomic numbers through LiTaO$_3$ to LiWO$_3$. These results support that the polar metals LiReO$_3$ and LiOsO$_3$ have short-range origins as suggested in Refs. [20–22]. We cannot distinguish the chemical and geometrical effect because we have not investigated the nature of chemical bondings around the Li ions.

The soft modes in these polar metals are dominated by the Li ions, while the electronic structures near the Fermi level consist of the O and B-site orbitals, which seems consistent with the decoupling electron mechanism. However, the weak coupling between the soft mode and the low-energy electronic structure does not prevent the screening of the long-range interactions, as suggested by Anderson and Blount [12]. Indeed, our calculations show that the unscreened interactions are not the main driving force of the instability of the high-symmetry $R\bar{3}c$ phases of the polar metals. However, this does not necessarily exclude the possibility that the remaining weak off-site interactions contribute to the emergence of the long-range order below T_c [25].

V. CONCLUSIONS

We perform a systematic analysis on LiBO$_3$ with $B =$ Ta, W, Re, Os. LiTaO$_3$ is a ferroelectric insulator, while LiReO$_3$ and LiOsO$_3$ are polar metals. The DFT calculations show that LiTaO$_3$ is an insulator while the other three are metals, consistent with the experiments. The phonon calculations show that the ferroelectriclike A_{2u} mode has the largest instability in the high-temperature $R\bar{3}c$ phase, consistent with the structural phase transitions. We then apply the SCPH-based structural optimization to LiBO$_3$ and accurately reproduce the chemical trend of the transition temperatures. From these calculations, we predict that LiWO$_3$ is another polar metal yet to be tested experimentally. In the end, we perform a detailed analysis on the interatomic force constants and explicitly show that the suppression of T_c in polar metals can be ascribed to the screening of the long-range IFCs caused by the itinerant electrons.

ACKNOWLEDGMENTS

This work was supported by JSPS KAKENHI Grants No. 21K03424 and No. 19H05825, Grant-in-Aid for JSPS Fellows (No. 22KJ1028), and JST-PRESTO (No. JPMJPR20L7 and No. JPMJPR23J6).

[1] Y. Shi, Y. Guo, X. Wang, A. J. Princep, D. Khalyavin, P. Manuel, Y. Michiue, A. Sato, K. Tsuda, S. Yu, M. Arai, Y. Shirako, M. Akaogi, N. Wang, K. Yamaura, and A. T. Boothroyd, A ferroelectric-like structural transition in a metal, Nature Mater. **12**, 1024 (2013).

[2] S. Bhowal and N. A. Spaldin, Polar metals: Principles and prospects, Annu. Rev. Mater. Res. **53**, 53 (2023).

[3] C. W. Rischau, X. Lin, C. P. Grams, D. Finck, S. Harms, J. Engelmayer, T. Lorenz, Y. Gallais, B. Fauqué, J. Hemberger, and K. Behnia, A ferroelectric quantum phase transition inside the superconducting dome of Sr$_{1-x}$Ca$_x$TiO$_{3-\delta}$, Nature Phys. **13**, 643 (2017).

[4] H. Takahashi, T. Akiba, K. Imura, T. Shiino, K. Deguchi, N. K. Sato, H. Sakai, M. S. Bahramy, and S. Ishiwata, Anticorrelation between polar lattice instability and superconductivity in the weyl semimetal candidate MoTe$_2$, Phys. Rev. B **95**, 100501(R) (2017).

[5] H. Sakai, K. Ikeura, M. S. Bahramy, N. Ogawa, D. Hashizume, J. Fujioka, Y. Tokura, and S. Ishiwata, Critical enhancement of thermopower in a chemically tuned polar semimetal MoTe$_2$, Sci. Adv. **2**, e1601378 (2016).

[6] H. Takahashi, K. Hasegawa, T. Akiba, H. Sakai, M. S. Bahramy, and S. Ishiwata, Giant enhancement of cryogenic thermopower by polar structural instability in the pressurized semimetal MoTe$_2$, Phys. Rev. B **100**, 195130 (2019).

[7] W. C. Yu, X. Zhou, F.-C. Chuang, S. A. Yang, H. Lin, and A. Bansil, Nonsymmorphic cubic dirac point and crossed nodal rings across the ferroelectric phase transition in LiOsO$_3$, Phys. Rev. Mater. **2**, 051201(R) (2018).

[8] P. Li, Y. Wen, X. He, Q. Zhang, C. Xia, Z.-M. Yu, S. A. Yang, Z. Zhu, H. N. Alshareef, and X.-X. Zhang, Evidence for topological type-II Weyl semimetal WTe$_2$, Nature Commun. **8**, 2150 (2017).

[9] W. Luo, K. Xu, and H. Xiang, Two-dimensional hyperferroelectric metals: A different route to ferromagnetic-ferroelectric multiferroics, Phys. Rev. B **96**, 235415 (2017).

[10] W. X. Zhou and A. Ariando, Review on ferroelectric/polar metals, Jpn. J. Appl. Phys. **59**, SI0802 (2020).

[11] D. Hickox-Young, D. Puggioni, and J. M. Rondinelli, Polar metals taxonomy for materials classification and discovery, Phys. Rev. Mater. **7**, 010301 (2023).

[12] P. W. Anderson and E. I. Blount, Symmetry considerations on martensitic transformations: "ferroelectric" metals? Phys. Rev. Lett. **14**, 217 (1965).

[13] W. Cochran, Crystal stability and the theory of ferroelectricity, Adv. Phys. **9**, 387 (1960).

[14] R. E. Cohen, Origin of ferroelectricity in perovskite oxides, Nature (London) **358**, 136 (1992).

[15] F. Jin, L. Wang, A. Zhang, J. Ji, Y. Shi, X. Wang, R. Yu, J. Zhang, E. W. Plummer, and Q. Zhang, Raman interrogation of the ferroelectric phase transition in polar metal LiOsO$_3$, Proc. Natl. Acad. Sci. **116**, 20322 (2019).

[16] F. Jin, A. Zhang, J. Ji, K. Liu, L. Wang, Y. Shi, Y. Tian, X. Ma, and Q. Zhang, Raman phonons in the ferroelectric-like metal LiOsO$_3$, Phys. Rev. B **93**, 064303 (2016).

[17] J.-Y. Shan, A. de la Torre, N. J. Laurita, L. Zhao, C. D. Dashwood, D. Puggioni, C. X. Wang, K. Yamaura, Y. Shi, J. M. Rondinelli, and D. Hsieh, Evidence for an extended critical fluctuation region above the polar ordering transition in LiOso$_3$, Phys. Rev. Res. **2**, 033174 (2020).

[18] H. Sim and B. G. Kim, First-principles study of octahedral tilting and ferroelectric-like transition in metallic LiOsO$_3$, Phys. Rev. B **89**, 201107(R) (2014).

[19] G. Giovannetti and M. Capone, Dual nature of the ferroelectric and metallic state in LiOsO$_3$, Phys. Rev. B **90**, 195113 (2014).

[20] H. J. Xiang, Origin of polar distortion in LiNbO$_3$-type "ferroelectric" metals: Role of A-site instability and short-range interactions, Phys. Rev. B **90**, 094108 (2014).

[21] N. A. Benedek and T. Birol, 'ferroelectric' metals reexamined: fundamental mechanisms and design considerations for new materials, J. Mater. Chem. C **4**, 4000 (2016).

[22] Q. Yao, H. Wu, K. Deng, and E. Kan, Ferroelectric-like structural transition in metallic LiOsO$_3$, RSC Adv. **4**, 26843 (2014).

[23] N. J. Laurita, A. Ron, J.-Y. Shan, D. Puggioni, N. Z. Koocher, K. Yamaura, Y. Shi, J. M. Rondinelli, and D. Hsieh, Evidence for the weakly coupled electron mechanism in an Anderson-Blount polar metal, Nature Commun. **10**, 3217 (2019).

[24] D. Puggioni and J. M. Rondinelli, Designing a robustly metallic noncenstrosymmetric ruthenate oxide with large thermopower anisotropy, Nature Commun. **5**, 3432 (2014).

[25] H. M. Liu, Y. P. Du, Y. L. Xie, J.-M. Liu, C.-G. Duan, and X. Wan, Metallic ferroelectricity induced by anisotropic

unscreened coulomb interaction in $LiOsO_3$, Phys. Rev. B **91**, 064104 (2015).

[26] K. F. Garrity, K. M. Rabe, and D. Vanderbilt, Hyperferroelectrics: Proper ferroelectrics with persistent polarization, Phys. Rev. Lett. **112**, 127601 (2014).

[27] P. Li, X. Ren, G.-C. Guo, and L. He, The origin of hyperferroelectricity in $LiBO_3$ (B = V, Nb, Ta, Os), Sci. Rep. **6**, 34085 (2016).

[28] S. Lei, M. Gu, D. Puggioni, G. Stone, J. Peng, J. Ge, Y. Wang, B. Wang, Y. Yuan, K. Wang, Z. Mao, J. M. Rondinelli, and V. Gopalan, Observation of quasi-two-dimensional polar domains and ferroelastic switching in a metal, $Ca_3Ru_2O_7$, Nano Lett. **18**, 3088 (2018).

[29] Z. Fei, W. Zhao, T. A. Palomaki, B. Sun, M. K. Miller, Z. Zhao, J. Yan, X. Xu, and D. H. Cobden, Ferroelectric switching of a two-dimensional metal, Nature (London) **560**, 336 (2018).

[30] Y. Wang, X. Liu, J. D. Burton, S. S. Jaswal, and E. Y. Tsymbal, Ferroelectric instability under screened coulomb interactions, Phys. Rev. Lett. **109**, 247601 (2012).

[31] X. He and K. J. Jin, Persistence of polar distortion with electron doping in lone-pair driven ferroelectrics, Phys. Rev. B **94**, 224107 (2016).

[32] H. J. Zhao, A. Filippetti, C. Escorihuela-Sayalero, P. Delugas, E. Canadell, L. Bellaiche, V. Fiorentini, and J. Íñiguez, Meta-screening and permanence of polar distortion in metallized ferroelectrics, Phys. Rev. B **97**, 054107 (2018).

[33] Y. Iwazaki, T. Suzuki, Y. Mizuno, and S. Tsuneyuki, Doping-induced phase transitions in ferroelectric $BaTiO_3$ from first-principles calculations, Phys. Rev. B **86**, 214103 (2012).

[34] K. Murayama, R. Masuki, H. Takatsu, C. Tassel, H. Sakai, X. Gu, K. Ishida, K. Denisova, V. Dupray, S. Clevers, T. Nomoto, T. Tadano, P. Lemmens, R. Arita, and H. Kageyama (unpublished).

[35] R. Masuki, T. Nomoto, R. Arita, and T. Tadano, *Ab initio* structural optimization at finite temperatures based on anharmonic phonon theory: Application to the structural phase transitions of $BaTiO_3$, Phys. Rev. B **106**, 224104 (2022).

[36] K. Ishida, Y. Ikeuchi, C. Tassel, H. Takatsu, C. M. Brown, and H. Kageyama, High-pressure synthesis of non-stoichiometric Li_xWO_3 ($0.5 \leqslant x \leqslant 1.0$) with $LiNbO_3$ structure, Inorganics **7**, 63 (2019).

[37] D. J. Hooton, The use of a model in anharmonic lattice dynamics, Philos. Mag. **3**, 49 (1958).

[38] N. S. Gillis, N. R. Werthamer, and T. R. Koehler, Properties of crystalline argon and neon in the self-consistent phonon approximation, Phys. Rev. **165**, 951 (1968).

[39] T. Tadano and W. A. Saidi, First-principles phonon quasiparticle theory applied to a strongly anharmonic halide perovskite, Phys. Rev. Lett. **129**, 185901 (2022).

[40] P. Souvatzis, O. Eriksson, M. Katsnelson, and S. Rudin, The self-consistent *ab initio* lattice dynamical method, Comput. Mater. Sci. **44**, 888 (2009).

[41] L. Monacelli, R. Bianco, M. Cherubini, M. Calandra, I. Errea, and F. Mauri, The stochastic self-consistent harmonic approximation: calculating vibrational properties of materials with full quantum and anharmonic effects, J. Phys.: Condens. Matter **33**, 363001 (2021).

[42] R. Masuki, T. Nomoto, R. Arita, and T. Tadano, Anharmonic Grüneisen theory based on self-consistent phonon theory: Impact of phonon-phonon interactions neglected in the quasiharmonic theory, Phys. Rev. B **105**, 064112 (2022).

[43] T. Tadano and S. Tsuneyuki, Self-consistent phonon calculations of lattice dynamical properties in cubic $SrTiO_3$ with first-principles anharmonic force constants, Phys. Rev. B **92**, 054301 (2015).

[44] R. Masuki, T. Nomoto, R. Arita, and T. Tadano, Full optimization of quasiharmonic free energy with an anharmonic lattice model: Application to thermal expansion and pyroelectricity of wurtzite GaN and ZnO, Phys. Rev. B **107**, 134119 (2023).

[45] D. C. Wallace, Thermodynamics of crystals, Am. J. Phys. **40**, 1718 (1972).

[46] T. Tadano, Y. Gohda, and S. Tsuneyuki, Anharmonic force constants extracted from first-principles molecular dynamics: applications to heat transfer simulations, J. Phys.: Condens. Matter **26**, 225402 (2014).

[47] Y. Oba, T. Tadano, R. Akashi, and S. Tsuneyuki, First-principles study of phonon anharmonicity and negative thermal expansion in ScF_3, Phys. Rev. Mater. **3**, 033601 (2019).

[48] F. Zhou, W. Nielson, Y. Xia, and V. Ozoliņš, Lattice anharmonicity and thermal conductivity from compressive sensing of first-principles calculations, Phys. Rev. Lett. **113**, 185501 (2014).

[49] G. Kresse and J. Furthmüller, Efficient iterative schemes for ab initio total-energy calculations using a plane-wave basis set, Phys. Rev. B **54**, 11169 (1996).

[50] J. P. Perdew, A. Ruzsinszky, G. I. Csonka, O. A. Vydrov, G. E. Scuseria, L. A. Constantin, X. Zhou, and K. Burke, Restoring the density-gradient expansion for exchange in solids and surfaces, Phys. Rev. Lett. **100**, 136406 (2008).

[51] P. E. Blöchl, Projector augmented-wave method, Phys. Rev. B **50**, 17953 (1994).

[52] G. Kresse and D. Joubert, From ultrasoft pseudopotentials to the projector augmented-wave method, Phys. Rev. B **59**, 1758 (1999).

[53] See Supplemental Material at http://link.aps.org/supplemental/10.1103/PhysRevB.110.094102 for the electronic structure calculations and harmonic phonon calculations of all B = Ta, W, Re, Os cases and also contains the detailed discussion on the difference between the ferroelectric insulators and polar metals, and some additional information.

[54] J.-S. Zhou, X. Li, J. M. He, J. Chen, and K. Yamaura, Strongly correlated electrons in the ferroelectric metal $LiOsO_3$, Phys. Rev. B **104**, 115130 (2021).

[55] I. Lo Vecchio, G. Giovannetti, M. Autore, P. Di Pietro, A. Perucchi, J. He, K. Yamaura, M. Capone, and S. Lupi, Electronic correlations in the ferroelectric metallic state of $LiOsO_3$, Phys. Rev. B **93**, 161113(R) (2016).

[56] P. Liu, J. He, B. Kim, S. Khmelevskyi, A. Toschi, G. Kresse, and C. Franchini, Comparative *ab initio* study of the structural, electronic, magnetic, and dynamical properties of $LiOsO_3$ and $NaOsO_3$, Phys. Rev. Mater. **4**, 045001 (2020).

[57] K. Momma and F. Izumi, *VESTA3* for three-dimensional visualization of crystal, volumetric and morphology data, J. Appl. Crystallogr. **44**, 1272 (2011).

[58] W. D. Johnston and I. P. Kaminow, Temperature dependence of raman and rayleigh scattering in $LiNbo_3$ and $LiTao_3$, Phys. Rev. **168**, 1045 (1968).